# Magnetotail Ion Structuring by Kinetic Ballooning-Interchange Instability

**Evgeny V. Panov[1,2]** [ID], **San Lu[3]** [ID], and **Philip L. Pritchett[4]** [ID]

[1]Space Research Institute, Austrian Academy of Sciences, Graz, Austria, [2]Institute of Physics, University of Graz, Graz, Austria, [3]CAS Center for Excellence in Comparative Planetology, CAS Key Laboratory of Geospace Environment, School of Earth and Space Sciences, University of Science and Technology of China, Hefei, China, [4]Department of Physics and Astronomy, University of California, Los Angeles, CA, USA

**Abstract** By combining three-probe THEMIS observations and 3-D Particle-in-Cell simulations, we identify key structures on the ion gyroradius scale that occur in connection with ballooning-interchange instability heads in the Earth's magnetotail. The mesoscale structures occur at sites of strong ion velocity shear and vorticity where the thermal ion Larmor radius is about half of the width of the head. Finer structures occur at the smaller scales characterizing the wavelength of the electromagnetic ion cyclotron waves generated at the heads. These two processes act to erode and thin the current sheet, thereby forming a local magnetotail configuration that is favorable for reconnection.

**Plain Language Summary** Ballooning-interchange heads are fundamental dynamic objects in the nightside Earth's magnetosphere, which represent magnetic structures that are similar in shape to the atmospheric mushroom clouds resulting from a sudden formation of a volume of lower-density gases. The heads appear in series and drive geomagnetic east-west oriented aurora, which glows like a pearl necklace across the night sky. Magnetospheric ions appear to sense the heads and modify their circular paths perpendicular to the magnetospheric magnetic field, because their gyration radius is on the order of the head's size. Such a modification of the ion motion appears to lead to ion redistribution on the two sides of the head according to the ion energy. Together with a finer ion structuring, which occurs along the magnetic field lines, these processes cause changes in the nightside magnetic field, which may lead to severe magnetospheric disturbances and prolonged bright aurora.

## 1. Introduction

The Solar System has long been extensively used as a natural laboratory to study numerous fundamental processes in collisionless plasmas. One of such processes is irregular gyromotion of ions at any persistent magnetic boundary or transient structure, whose spatial scale is comparable to thermal ion gyroradius. Emerging from such an ion motion, non-diagonal ion pressure tensor elements drive finite Larmor radius (FLR) effects (Rosenbluth & Simon, 1965; Stasiewicz, 1993), which may result in non-negligible electric fields due to charge separation.

Being not yet thoroughly investigated theoretically and observationally, these processes are of particular interest at transient northward magnetic field ($B_Z$) intensifications (dipolarization fronts; DFs) (Nakamura et al., 2002; Russell et al., 1998; Sundberg et al., 2012) in the tails of planetary magnetospheres. DFs are embedded in mesoscale ion bursty bulk flows, or BBFs (Angelopoulos et al., 1994; Baumjohann et al., 1990). Being part of global circulation of the magnetospheric magnetic flux (Dungey, 1961; Vasyliunas, 1983), BBFs/DFs contribute to tailward expansion of the dipolarized region of the magnetotail (Baumjohann et al., 1999; Merkin et al., 2019).

BBFs/DFs are often attributed to magnetic reconnection outflows (Angelopoulos et al., 2008; Coppi et al., 1966) and are indeed found to exhibit prominent FLR effects at the stage of their propagation to and interaction with the dipole magnetic field lines of the Earth's magnetosphere (Pritchett, 2015; Pritchett & Runov, 2017; Sergeev et al., 2009). Alternatively, BBFs could be generated by various interchange processes (Rosenbluth & Longmire, 1957). Confirming this, recent results suggest that kinetic (electron) ballooning-interchange instability (BICI) (Panov, Nakamura, et al., 2012; Panov, Sergeev, et al., 2012; Panov & Pritchett, 2018a; Pritchett & Coroniti, 2010, 2013; Pritchett et al., 2014) could drive moderate ion flows during detachments of single or multiple BICI heads in the near-Earth's magnetotail. The latter fact follows from many in situ BICI signatures observed by THEMIS spacecraft that were predicted by Particle-In-Cell (PIC) simulations (Panov et al., 2020), as well as from

indirect signatures provided by ground All-Sky-Imager observations of auroral beads and rays, when single beads or rays lighted up simultaneously with prominent DFs, which were observed by THEMIS spacecraft amidst long chains of azimuthally drifting BICI heads (Panov et al., 2019). Such dipolarization fronts have been interpreted as leading edges of BICI heads detaching from the magnetotail region with reversed $B_Z$ gradient, the latter being the driver of the BICI instability.

A BICI head detachment progressively builds up ion velocity shears at two head's sides, being part of a dual ion vortex system formed asymmetrically with a larger vortex on the duskside of a dawnward propagating head (Panov et al., 2020). Taking into account typical azimuthal scales of the BICI head and sizes of two side vortices of about 1–2 Earth's radii ($R_E$) we expect that a significant portion of ions from the magnetotail plasma sheet exhibit agyrotropic rotation in the vicinity of BICI heads. Moreover, such motions should be asymmetric on the dusk- and dawnsides of BICI heads due to $\omega \cdot \mathbf{b}$ asymmetry of ion FLR effects (Cerri, 2018; Del Sarto et al., 2016; Franci et al., 2016; Huba, 1996; Markovskii et al., 2006; Parashar & Matthaeus, 2016; Yang et al., 2017).

At smaller scales, the BICI heads were found to be rippled by strong off-equator waves with frequency of the order of the ion gyrofrequency (Panov & Pritchett, 2018b; Pritchett et al., 2014), matching the properties of the left hand polarized and strongly compressional electromagnetic ion cyclotron waves (Perraut et al., 2000). These waves appeared due to strong differential electron-ion drift propagated azimuthally with speeds of a fraction of $V_{Ti}$, the ion thermal speed.

Here we investigate ion structures that occur due to agyrotropic rotation of ions and electromagnetic ion cyclotron waves by comparing ions' behavior predicted by the simulation with those collected in situ, when a head developed at the location of three THEMIS probes. We use burst mode three-point THEMIS (Angelopoulos, 2008) observations on a rare occasion, when the bulk of thermal ion population was well within the operational energy range of THEMIS electrostatic analyzers' (ESA) (McFadden et al., 2008) particle detectors, with ion distribution functions sampled once every 3 s. We further improved the quality of the ion data using measurements from Solid State Telescopes (SST) for energetic ions by combining the ESA and SST distribution functions and ion moments. For our analysis, we used 128 Hz resolution electromagnetic fields data from the THEMIS fluxgate magnetometers (FGM) (Auster et al., 2008) and electric field (EFI) instruments (Bonnell et al., 2008).

## 2. Comparision of THEMIS and PIC Data

The top panel in Figure 1 shows joint SST (full mode) and ESA (burst mode) ion differential flux spectra as observed by THEMIS probe P4 on 19 May 2010 (Figures S1 and S2 in Supporting Information S1 show the corresponding data for probes P3 and P5 in the same layout). THEMIS data are shown in geocentric solar magnetospheric (GSM) or Despun, Sun-pointing, L-momentum vector (DSL) (electric field) coordinates. In the spectra, average ion temperature is overplotted by the green curve. The temperature increased after 12:12 UT, when the lack of lower-energy ions and admixture of higher-energy ions was observed (black arrow in the panel). The second panel in Figure 1 shows the ion differential flux distribution depending on the azimuthal (PHI) angle of ion motion. The panel reveals both Earthward (PHI = 0,360) and tailward (PHI = 180) moving ion populations. The dominant Earthward ion population was observed before 12:12:30 UT (denoted by the vertical black line at the time when the ion $V_{iX}$ velocity component went through zero—cf. fifth panel), which changed to the dominant tailward ion population later. An Earthward-to-tailward ion flow reversal is a persistent feature of a BICI head at a later stage of development, which appears due to a dawn-to-dusk spacecraft trajectory through the head (Panov et al., 2020).

The Earthward and tailward ion flows were not uniform, as there were also observed minor tailward ion populations before 12:12:30 UT and minor Earthward ion populations after 12:12:30 UT. We show that an admixture of ion populations, which were moving opposite to the direction of the net ion flow, were due to the electromagnetic ion-cyclotron waves, which may be generated at BICI heads (Pritchett et al., 2014). The minor tailward ion populations were especially pronounced inside a lower-density interval (density trough) between 12:12 and 12:12:30 UT (see burst mode 128 samples per second spacecraft potential data from EFI in the 3d panel, which is a high-resolution proxy to the electron density). In the density trough, the ion temperature exhibited an increase of a factor of two with respect to the background ion temperature (temperature hump in the fourth panel). These minor tailward ion populations are associated with the local minima in the temperature hump and with the minima in $V_{iX}$ (indicated by four vertical dashed black lines). EFI 3s-sliding window averaged $E_Z$ electric field component
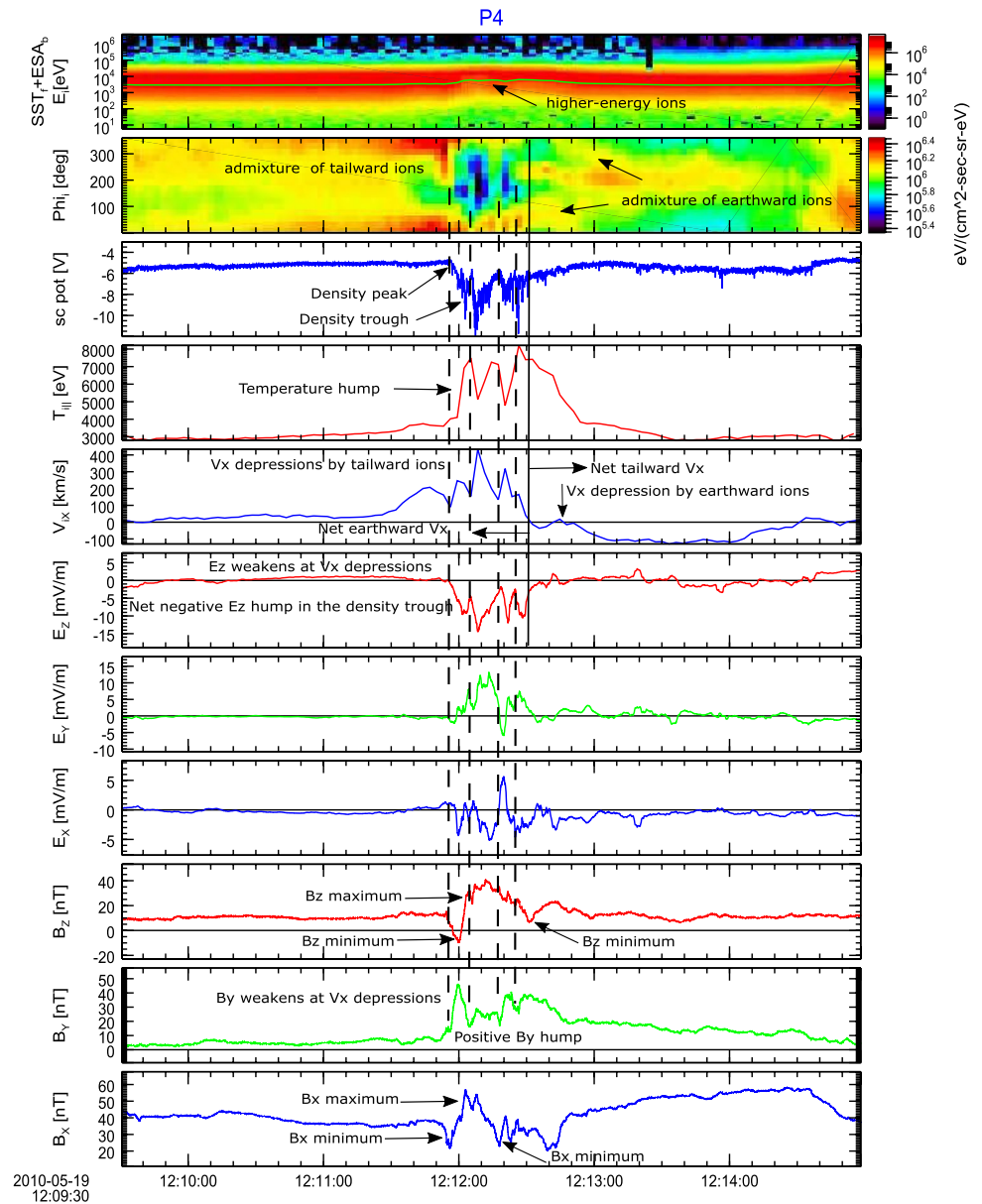
**Figure 1.** Time History of Events and Macroscale Interactions during Substorms (THEMIS) probe P4 observations on 19 May 2010 between 12:09:30 and 12:15 UT. From top to bottom are shown: joint Solid State Telescope (full mode) and THEMIS electrostatic analyzer (burst mode) ion differential flux spectra, azimuthal (PHI; 0° corresponds to the Earthward direction) angle of ion velocity, spacecraft potential (a high-resolution proxy to electron density), parallel component of the ion temperature (red), geocentric solar magnetospheric (GSM) $V_X$ ion velocity component, DSL $E_Z$ (red), $E_Y$ (green) and $E_X$ (blue) electric field components 3s-long-sliding-window averaged, GSM $B_Z$ (red), $B_Y$ (green) and $B_X$ (blue) magnetic field components.

revealed a negative hump associated with the density trough (negative $E_z$ hump in sixth panel; electric field is shown in DSL coordinates, which was close to GSM). This hump is a signature of a current sheet charging. The minor tailward ion populations coincide with local depressions of the negative $E_z$ hump (vertical dashed black lines). Two other electric field components (panels 7 and 8) indicate a net duskward $E_Y$ and variations in $E_X$. GSM magnetic field components (panels 9–11) reveal larger-scale variations related to the density trough/temperature hump, and smaller-scale variations. The smaller scale variations in $B_Z$ and $B_Y$ (panels 9 and 10) appeared to be anti-correlated, and probably related to the minor ion populations (e.g., minima in $B_Y$ correspond to the minima in $V_{iX}$). Similar (but time shifted) larger-scale variations in $B_Z$ and $B_X$ sequentially exhibiting minima, then maxima
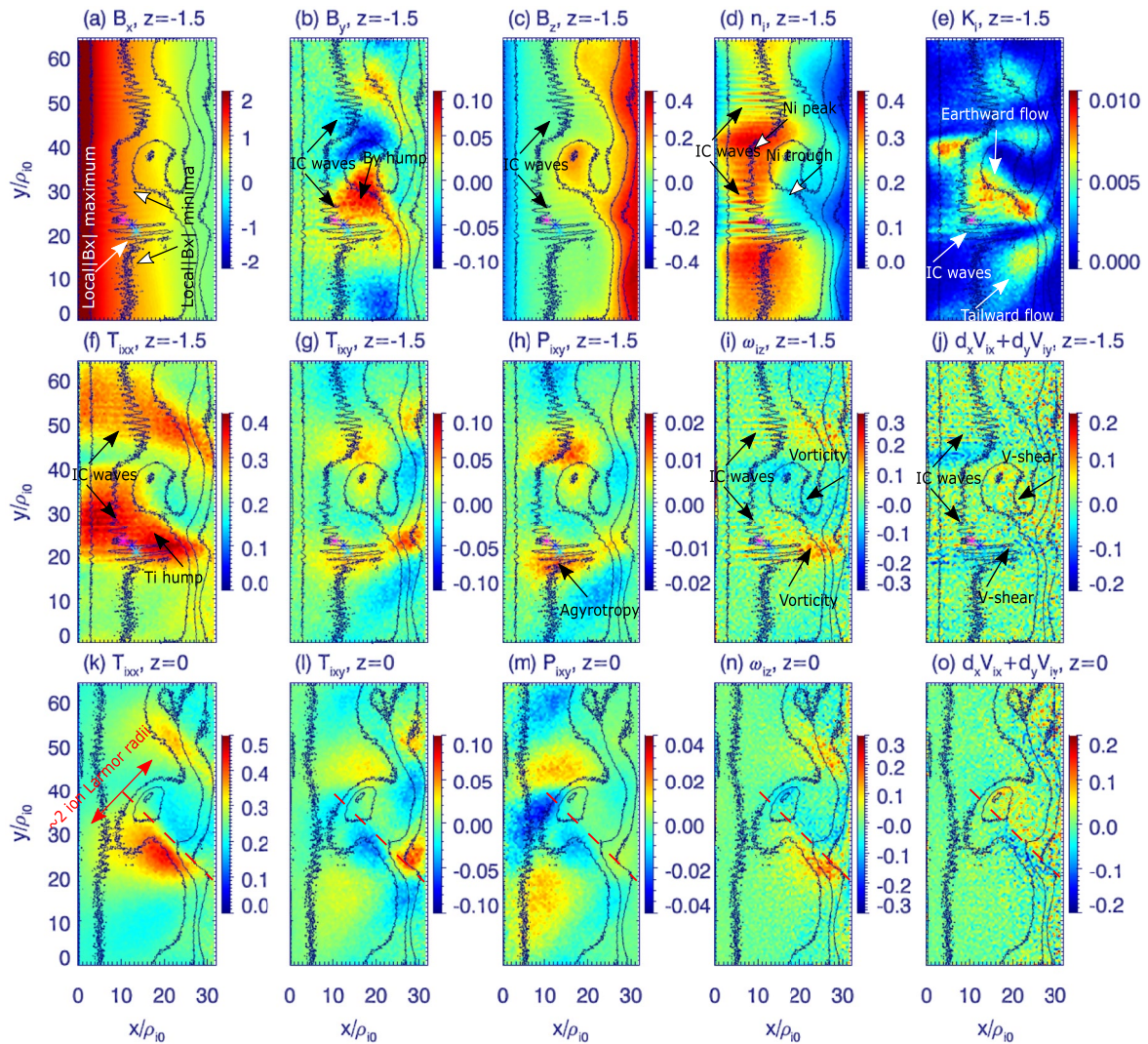
**Figure 2.** The later-stage ($\Omega_{i0}t = 210$) development of the ballooning-interchange instability in the xy (equatorial) southern hemisphere ($z = -1.5$) and neutral ($z = 0$) planes with the emergence of two ballooning-interchange instability heads predicted by 3-D Particle-In-Cell simulation using the electron (charged) current sheet. The x coordinate is directed tailward. The y coordinate is directed toward dawn. The coordinates are expressed in $\rho_{i0}$—the ion gyroradius in the asymptotic lobe $B_0$ field. The black contours show levels of $B_z$ in each panel. The following field and plasma quantities are shown in the figure: three magnetic field components (a, b, c), ion density (d), ion kinetic energy (e), ion temperature tensor $T_{xx}$ and $T_{xy}$ elements (f, g), $P_{xy}$ ion pressure tensor element (h), out-of-plane component of curl of the ion velocity (i), equatorial component of divergence of ion velocity (j). Panels (k) through (o) show the same simulation quantities as panels (f) through (j) at $z = 0$. The dashed red lines in the bottom row approximately divide the ballooning-interchange instability head into dusk (below the lines) and dawn (above the lines) parts.

and again minima (highlighted by the black arrows) coexisted with a broad net positive hump in $B_Y$ between 12:12 and 12:12:45 UT. $B_X$ was the main field component (bottom panel), whose variations opposed those in the electron density (third panel). These larger-scale variations were observed by virtual spacecraft in the following BICI simulations.

We use the PIC simulation run of a BICI head, for which the setup conditions were explained in Appendix 1 of Panov and Pritchett (2018b); reproduced in PIC Simulation Setup Section in the Supporting Information S1. Figure 2 shows instantaneous development of various field and ion quantities at $\Omega_{i0}t = 210$, where $\Omega_{0i}$ is the proton gyrofrequency. The most pronounced BICI head is seen around $y/\rho_{i0} = 30$ as a reddish $B_z$ spot (panel c), being partly detached from the tailward $B_z$ gradient ($20 < x/\rho_i < 27$). This head drifted dawnward and grew Earthward (cf. Movie S1 for a continuous development between $\Omega_{i0}t = 161$ and $\Omega_{i0}t = 280$). Duskward from the head (around $y/\rho_{i0} = 20$) were observed electromagnetic ion-cyclotron waves, driven by the ion-electron differential drift (Panov & Pritchett, 2018b; Pritchett et al., 2014); the drift is not shown in the present paper. Similar

waves (around $y/\rho_{i0} = 50$) belong to the duskside of the less pronounced head around $y/\rho_{i0} = 60$. There were also observed $B_x$ and $B_y$ variations associated with both, the BICI head and the ion-cyclotron waves, as seen in panels (a, b). A density enhancement and depression (panel d) was observed in front and behind the reddish $B_z$ spot ($N_i$ peak and trough). At this stage, the ion-cyclotron waves significantly modify the structure of the ion flow on the duskside of the head between the Earthward and tailward flows (panel e). In this place, there was also an increase in the ion temperature ($T_i$ hump in panel f). Associated with the hump, non-diagonal ion temperature tensor $T_{xy}$ (g) and ion pressure tensor $P_{xy}$ (h) elements being the result of anisotropy in ion velocity distribution function revealed significant agyrotropy in the ion motion caused by decoupling of ion motion from the magnetic field. The agyrotropic ion motion occurred at the locations of ion flow vorticity (panel i), and of the ion flow divergence (panel j). The bottom row in Figure 2 repeats its middle row for $z = 0$ (instead of $z = -1.5$). Although the results are similar to those in the middle row, the quantities at $z = 0$ exhibited more axial symmetry on the two sides of the head: above and below the dashed red lines. The explanation for this is that the ion patterns at $z = -1.5$ were more duskward than those at $z = 0$, which is also seen in Figure 4d below. $T_{xy}$ and $P_{xy}$ appeared to be the dominant non-diagonal temperature and pressure tensor elements at $z = 0$ (not shown). According to Figure S6b in the PIC Simulation Setup Section of the Supporting Information S1, the equatorial $B_z$ magnetic field was ~0.1 of the asymptotic lobe $B_0$ field (for $x/\rho_{i0}$ between 10 and 20), suggesting the ion gyroradius in the equatorial plane ~$10\rho_{i0}$. Hence, the width of the simulated BICI head was about 2 ion Larmor radii in the equatorial $B_z$ magnetic field (Figure 2k).

With the help of Figure 3 we compare the three-point THEMIS observations (right column) from Figure 1 and Figures S1 and S2 in Supporting Information S1 with virtual spacecraft observations at three locations in the PIC simulation domain (left column), that are indicated by the cyan, blue and magenta glyphs in each panel of Figure 2. The exact locations of the three glyphs are indicated on the top of the left column. Due to the opposite direction of the $x$ and $y$ axes in the simulation box as compared to the GSM coordinates, the three virtual spacecraft observations are shown for the southern hemisphere. The corresponding virtual spacecraft observations in the northern hemisphere are provided in Figure S3 in Supporting Information S1. The right column shows data from three THEMIS probes on 19 May 2010 between 12:10 and 12:14 UT. In each panel cyan curve stands for P3, blue—for P4 and magenta—for P5. Probes' locations in $R_E$ GSM are provided on the top of the column. The barycenter of the probes was near $(-8; 1; 3)$ $R_E$ GSM. Radially, P5 was about 2,000 km more Earthward than P3/P4; azimuthally P4 was between P3 on the duskside and P5 on the dawnside. Such configuration of the three probes is close (in relative probe location, inter-probe scales and timing/sequence of magnetotail observation) to those of the virtual spacecraft indicated by three glyphs in Figure 2.

The most pronounced structure (seen in the $B_X$ GSM magnetic field component; first panel in the right column in Figure 3) reveals a local $B_X$ peak around 12:12:15 UT, which was surrounded by two minima before and after the peak. This major structure was clearly reproduced in the simulation $B_x$ on the left, as was the net positive hump in the simulation $B_y$ as in the observed $B_Y$ GSM on the right (second panels). The smaller scale shape of $B_Y$ and $B_Z$ GSM (second and 3d panels on the right) curves appeared to be anticorrelated (maxima in $B_Y$ correspond to minima in $B_Z$ and vice versa). Due to numerical noise, these smaller scale variations were difficult to reproduce in simulation $B_y$ and $B_z$. The larger scale behavior of the simulation $B_z$ still reproduced the maximum and minima features in $B_Z$ GSM on the right. The total magnetic field $B_{\text{total}}$ ($B_t$ and $B_T$ in the fourth panels from the top) repeated the main features of $B_X$ (a maximum between two minima). From the magnetic field, we were able to identify the propagation velocity of the $B_T$ maximum in the THEMIS data with the help of the timing method (Russell et al., 1983), which was applied to the sharp magnetic boundary in $B_T$ data around 12:12 UT using time delays in observation of this feature between three THEMIS probes. The magnetotail $B_T$ maximum appeared to move mainly dawnward along the unit vector $N_{XY} = (0.014; -0.999;$ GSM$)$, at a velocity $V_N \approx 70.9$ km/s. Knowing $V_N$ one can evaluate the azimuthal scale of the head of about 2,130 km (the duration of the $B_T$ maximum was ~30 s). The ion $V_X$ and $V_Y$ velocity components (fifth and sixth panels in Figure 3) exhibited Earthward and duskward flow around 12:12:15 UT. Around 12:12:45 UT $V_X$ and $V_Y$ reversed signs.

The dawnside of the BICI head in the simulation (which was observed before $\Omega_i t \approx 215$) appeared to contain a denser and cooler plasma (panels 7 and 8 in the left column of Figure 3), whereas the duskside exhibited lack of plasma and enhanced ion temperature (after $\Omega_i t \approx 215$ in the same panels). Due to delay of more than $30\Omega_i t$ in virtual probes observation of the head's dawn- and duskside, the temperature on the duskside changed more dramatically from the initial ion temperature than on the dawnside. A similar density trough with an ion temperature
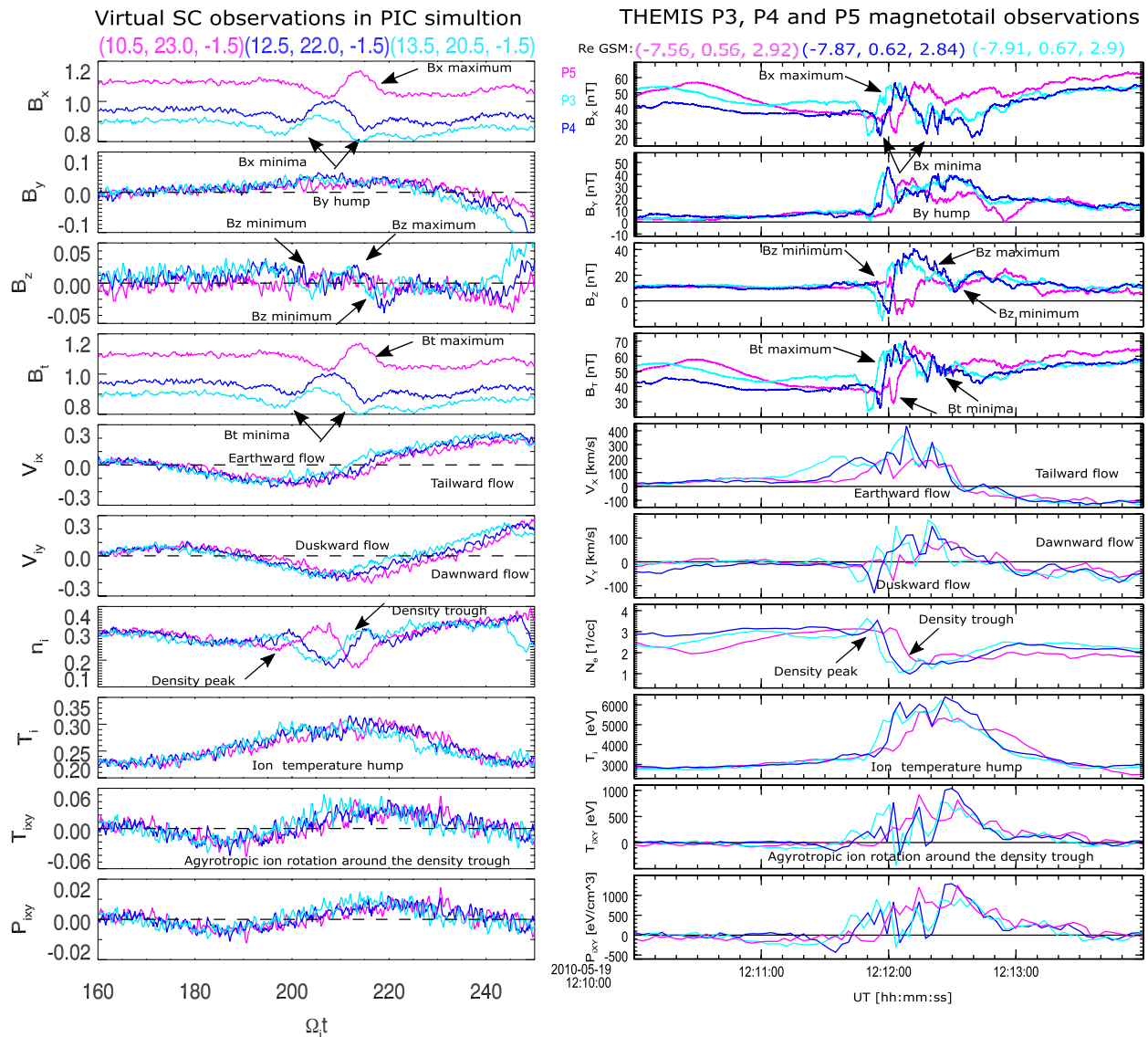
**Figure 3.** Comparison of ballooning-interchange instability (BICI) head observations by three virtual spacecraft in the 3D Particle-In-Cell simulation box (left column) and by three Time History of Events and Macroscale Interactions during Substorms (THEMIS) probes in the Earth's magnetotail (right column). Locations of the virtual spacecraft and THEMIS probes are provided in tops of the two columns. Results from 3D PIC simulation of BICI development in the electron (charged) current sheet between $\Omega_{i0}t = 160$ and $\Omega_{i0}t = 250$ are (left column; from top to bottom) three magnetic field components and the total magnetic field $(B_x, B_y, B_z, B_t)$, X and Y ion velocity components $V_{ix}$ and $V_{iy}$, ion density $N_i$, average ion temperature $T_i$, non-diagonal ion temperature and ion pressure tensor elements $T_{ixy}$ and $P_{ixy}$. In the simulation, the *X* axis is directed antisuward and the *Y* axis is dawnward, which is opposite to the GSM *X* and *Y* axes. The three curves correspond to the location of three virtual spacecraft at $(x/\rho_{i0},y/\rho_{i0},z/\rho_{i0}) = (10.5,23.0,-1.5)$ (magenta), at $(x/\rho_{i0},y/\rho_{i0},z/\rho_{i0}) = (12.5,22.0,-1.5)$ (blue) and at $(x/\rho_{i0},y/\rho_{i0},z/\rho_{i0}) = (13.5,20.5,-1.5)$ (cyan). Figure S3 in Supporting Information S1 shows the simulation data at the same X and Y positions, but in the opposite Z-location $(z = 1.5)$. Three THEMIS probes' observations on 19 May 2010 between 12:10 and 12:14 UT by probes P3 (cyan), P4 (blue) and P5 (magenta) (right column; from top to bottom) are three geocentric solar magnetospheric (GSM) and total magnetic field components $(B_X, B_Y, B_Z, B_T)$, X and Y (GSM) ion velocity components $V_X$ and $V_Y$, electron density $N_e$ (we assume quasi-neutrality of plasma here; the ion density from the joint THEMIS electrostatic analyzer-Solid State Telescope data underestimated the actual plasma density by up to 20%), average ion temperature $T_i$, non-diagonal ion temperature and ion pressure tensor elements $T_{XY}$ and $P_{XY}$.

hump was sensed by THEMIS around 12:12:30 UT (panels 7 and 8 in the right column of Figure 3). The last four panels at the bottom of Figure 3 show xy temperature and pressure tensor elements. Both virtual spacecraft and THEMIS probe observations consistently exhibited significant non-diagonal ion temperature and ion pressure tensor elements around the temperature hump (simulated $T_{xy}$ and $P_{xy}$ features appeared periodically together with arrivals of new heads). All THEMIS signatures indicated in the right column were accurately reproduced by the PIC simulations in the left column (disturbances related to the ion-cyclotron waves were not indicated
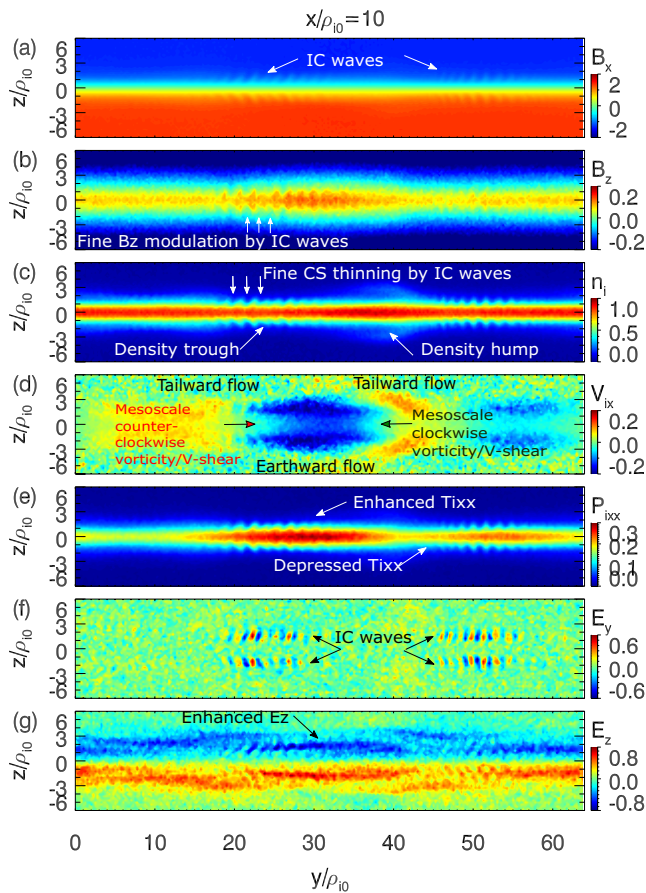
**Figure 4.** Results from the same 3D Particle-In-Cell simulation as in Figure 2 in the yz plane at $x/\rho_{i0} = 10$: $B_x$ (a) and $B_z$ (b) magnetic field components, ion density (c), ion velocity $V_{ix}$ component (d), $P_{xx}$ ion pressure tensor component (e), $E_y$ (f) and $E_z$ (g) electric field component. The coordinates are expressed in $\rho_{i0}$—the ion gyroradius in the asymptotic lobe $B_0$ field.

in Figure 3, because they were not well seen in the simulation data due to numerical noise).

Figure 4 shows simulation results in the yz (cross-tail) slices at $x/\rho_{i0} = 10$. The middle head is seen in the pronounced Earthward flow (bluish $V_{ix}$ spot in panel d), which was drifting to the right (dawnward). The places of mesoscale velocity shears are present on the two sides of the Earthward flow between the bluish and yellowish spots. The density trough (panel c) containing hotter ion population (and larger pressure, panel e) appears at the duskside of the Earthward flow. It is this region, which was observed as peaks in $B_x$ and $B_t$ in Figure 3, which gets thinner (also with time) than the surrounding current sheet. A further thinning of this region at smaller scales was provided by the ion-cyclotron waves, which were localized between the neutral sheet and the lobes around $z/\rho_{i0} = \pm 1.4$. In these locations, the waves modulated $B_z$ (b), ion density and pressure (c, e), as well as $E_z$ (g). The appearance of both the density trough and the ion-cyclotron waves acted to create regions, in which the current sheet tended to become locally one-dimensional (with a decreased $B_z$). Complementary to panels (f, g) in Figure 4, Figure S4 from the Supporting Information S1 shows the xy slices of the $E_y$ and $E_z$ in the same format as panels in Figure 2. Figure S4 in Supporting Information S1 reveals the radial extent of the electric component of the ion-cyclotron waves ($E_y$) and the distribution of the current sheet charging ($E_z$). The ion-cyclotron waves also produce ion velocity shears on the scales of the wave length (horizontal stripes in Figure 2e produced by both $V_{ix}$ and $V_{iy}$).

Figure 5 is aimed at identification of regions with stronger vorticity at two heads' sides that are indicated in panel (d) of Figure 4. The top and the second panels in Figure 5 show the Z GSM component of the ion vorticity $\omega_Z$ and components of the ion divergence (of which $\partial V_{iy}/\partial y$ appeared to be the major component; green curve), which were calculated using three spacecraft P3–P5 data. A clear and prominent region of the mesoscale clockwise vorticity and velocity shear was observed at the dawnward side of the head (before 12:11:40 UT). As the head drifted dawnward, the three probes started to observe the duskward side of the head. In addition to an average counter-clockwise sense of rotation of the ion flows after 12:11:40 UT, the probes also observed significant flow variability of a smaller duration. These smaller

scale variations in $\omega_Z$ and div(V) are related to the minor tailward-moving ion populations shown in the second panel of Figure 1. They can be explained by the presence of the ion-cyclotron waves on the duskside of the head. Starting from the third panel, the color coding of Figure 5 is the same as in the right column of Figure 3. This part of Figure 5 allows to understand the observed current sheet dynamics in the location of the density trough (third panel in Figure 5). In the trough, both the magnetic field pressure (fourth panel) and the sum of the magnetic and the plasma pressure $P_p + P_B$ (fifth panel) significantly increased, leading to a drop in the plasma-to-magnetic pressure ratio (plasma $\beta = P_p/P_B$; sixth panel). Thus, the trough appeared to be formed inside a locally thinning current sheet, with charging being accumulated (cf. $E_z$ in seventh panel in Figure 5). Taking $P_p + P_B = 1.6$ nPa and $B_T = 50$ nT at 12:10UT, the magnetotail lobe field $B_0$ was ~63 nT, and the ion gyroradius in the lobe magnetic field ~88 km (assuming $T_i = 3$ keV), being an observational analogue of $\rho_{i0}$ in the simulation plots. A lower estimate of the equatorial ion gyroradius of ~554 km comes from the observed $B_z$ ~10 nT.

After the present THEMIS observations (cf. Figure S5 in Supporting Information S1) we identified two additional heads (denoted as BI head 2, 3 around 12:15:40 UT and 12:17 UT), in addition to the present head (denoted as BI head 1 around 12:12 UT). Both additionally identified heads exhibit less pronounced, but still easily recognizable signatures of the present head, such as the density troughs, the temperature humps, the Earthward flows and the magnetic field variations, being consistent with the multiple appearance of the BICI heads at different stage of development in the simulation (cf. Figure 2, around $y/\rho_{i0} = 58$; we could not identify the ion-cyclotron signatures in the ion data for the additional BI heads, probably due to insufficient time resolution of the data).
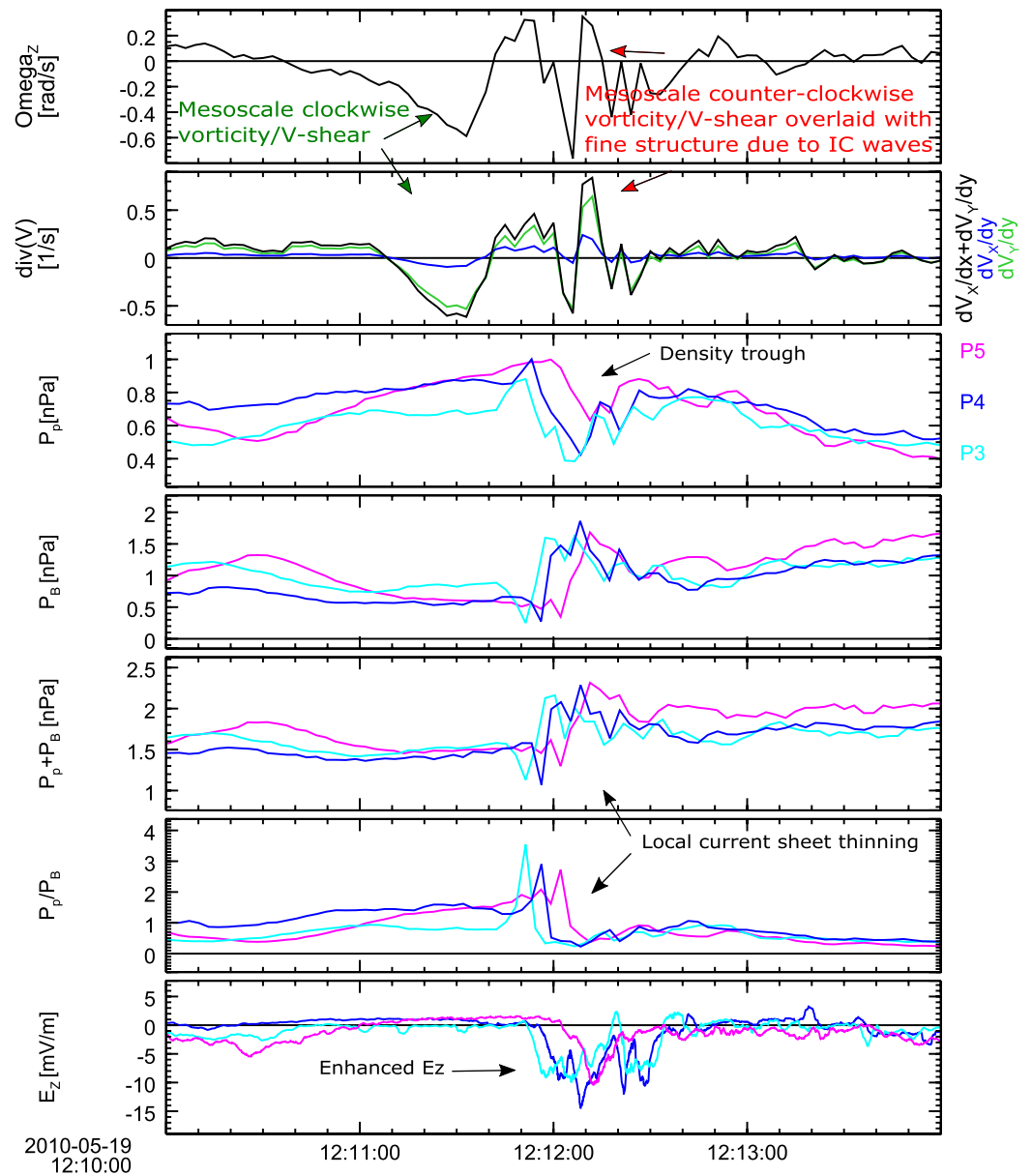
**Figure 5.** Time History of Events and Macroscale Interactions during Substorms (THEMIS) probes P3–P5 observations on 19 May 2010 between 12:10 and 12:14 UT. From top to bottom are shown: z component of curl of the ion velocity $\omega_z$ and equatorial components of divergence of the ion velocity – $\partial V_{ix}/\partial x$ (blue), $\partial V_{iy}/\partial y$ (green) and the sum of the two (black). $\omega_z$, $\partial V_{ix}/\partial x$ and $\partial V_{iy}/\partial y$ were calculated for the area of the triangle with its apices at the locations of P3, P4, and P5 (coordinates are provided in the top of the right panel in Figure 3; the triangle is shown in Figure S3 of the Supporting Information S1). Ion pressure $P_p$, magnetic field pressure $P_B$, sum of the ion and magnetic field pressures, ion-to-magnetic pressure ratio (plasma $\beta = P_p/P_B$), vertical component of the electric field $E_Z$ at probes P3 (cyan), P4 (blue) and P5 (magenta). All shown parameters are derived from joint THEMIS electrostatic analyzer-Solid State Telescope ion observations.

## 3. Conclusive Discussion

Ions operate in BICI processes at two scales. Mesoscale ion dynamics was observed as agyrotropic ions' rotation at the head of a cross-tail size of the order of the thermal ion gyroradius. This ion behavior is presumably stipulated by vorticity and flow shears at the sides of the head. Both observations and the simulation indicate humps (reductions) in the ion temperature (density) on the duskside of the heads, and ion temperature reductions (density humps) on the dawnside. The humps and reductions appear in the regions of strong velocity shears/vorticity between the head's Earthward and side tailward flows on head's two sides. There, ion agyrotropic motion

occurred asymmetrically. Since vorticity on the duskside was opposite to the ion gyromotion, the penetrating from the dawnside higher-energy ions are expected to experience braking and remain on the duskside. Opposite to that, the higher-energy ions penetrating from the duskside into the dawnside might be accelerated by the dawnside vortex, which has the same sense of rotation as the ion gyromotion. Such ions might be able to gain sufficient velocity to escape from the dawnside vortex, for example, further dawnward. Thus, it is the penetration of the superthermal ions from the dawnside across the head to the duskside that is responsible for the enhancement in the observed ion temperature on the duskside of the head. In turn, the dawnside ion temperature decreases due to escape of higher energy ions from the dawnside vortex. This phenomenon is known as $\boldsymbol{\omega} \cdot \mathbf{b}$ asymmetry of ion FLR effects (Cerri, 2018; Del Sarto et al., 2016; Huba, 1996; Franci et al., 2016; Markovskii et al., 2006; Parashar & Matthaeus, 2016; Yang et al., 2017). The $\boldsymbol{\omega} \cdot \mathbf{b}$ asymmetry of BICI DFs is expected to complement the known ion FLR effects with non-significant vorticity during DF interaction with Earth's dipolar field lines (Pritchett & Runov, 2017; Sergeev et al., 2009).

The ions' patterns were further modulated at smaller scales by the electromagnetic ion-cyclotron waves. In the simulation, the waves were observed in the density trough/temperature hump regions in Figure 2. In THEMIS observations, the waves were identified as tailward ion populations around $PHI_i = 180$ (or alternatively modulated Earthward ion population near $PHI_i = 0$) around 12:12 UT in the second panel of Figure 1. The waves were responsible for local depressions of temperature in the temperature hump, as well as for local reduction of Earthward $V_X$ and the negative $E_Z$ hump (cf. Figures 1 and 4).

Both processes lead to the local current sheet deformations at their characteristic scales. At the head's duskside, the deformations started off-equator locally compressing the current sheet. There, $B_Z$ became significantly smaller and even negative ($B_Z$ field was still positive everywhere at $z = 0$, indicating that there has been no onset of reconnection). Because such current sheet deformations progressed toward the neutral sheet plane with time (cf. Movie S1), the temperature hump formation and growth of electromagnetic ion-cyclotron waves are potential mechanisms for forcing current sheet reconnection locally and in a competitive manner at a later stage of BICI development, as predicted by the earlier simulations (Pritchett & Coroniti, 2011, 2013).

## Data Availability Statement

Data sets used for producing the figures are available at the website https://doi.org/10.6084/m9.figshare.16910098.v2.

## References

Angelopoulos, V. (2008). The THEMIS mission. *Space Science Reviews*, *141*, 5–34. https://doi.org/10.1007/s11214-008-9336-1

Angelopoulos, V., Kennel, C. F., Coroniti, F. V., Pellat, R., Kivelson, M. G., Walker, R. J., et al. (1994). Statistical characteristics of bursty bulk flow events. *Journal of Geophysical Research*, *99*, 21. https://doi.org/10.1029/94JA01263

Angelopoulos, V., McFadden, J. P., Larson, D., Carlson, C. W., Mende, S. B., Frey, H., et al. (2008). Tail reconnection triggering substorm onset. *Science*, *321*, 931–935. https://doi.org/10.1126/science.1160495

Auster, H. U., Glassmeier, K. H., Magnes, W., Aydogar, O., Baumjohann, W., Constantinescu, D., et al. (2008). The THEMIS fluxgate magnetometer. *Space Science Reviews*, *141*, 235–264. https://doi.org/10.1007/s11214-008-9365-9

Baumjohann, W., Hesse, M., Kokubun, S., Mukai, T., Nagai, T., & Petrukovich, A. A. (1999). Substorm dipolarization and recovery. *Journal of Geophysical Research*, *104*, 24995–25000. https://doi.org/10.1029/1999JA900282

Baumjohann, W., Paschmann, G., & Luehr, H. (1990). Characteristics of high-speed ion flows in the plasma sheet. *Journal of Geophysical Research*, *95*, 3801–3809. https://doi.org/10.1029/JA095iA04p03801

Bonnell, J. W., Mozer, F. S., Delory, G. T., Hull, A. J., Ergun, R. E., Cully, C. M., et al. (2008). The electric field instrument (EFI) for THEMIS. *Space Science Reviews*, *141*, 303–341. https://doi.org/10.1007/s11214-008-9469-2

Cerri, S. S. (2018). Finite-larmor-radius equilibrium and currents of the earth's flank magnetopause. *Journal of Plasma Physics*, *84*(5), 555840501. https://doi.org/10.1017/S0022377818000934

Coppi, B., Laval, G., & Pellat, R. (1966). Dynamics of the geomagnetic tail. *Physical Review Letters*, *16*, 1207–1210. https://doi.org/10.1103/PhysRevLett.16.1207

Del Sarto, D., Pegoraro, F., & Califano, F. (2016). Pressure anisotropy and small spatial scales induced by velocity shear. *Physical Review E - Statistical Physics, Plasmas, Fluids, and Related Interdisciplinary Topics*, *93*, 053203. https://doi.org/10.1103/PhysRevE.93.053203

Dungey, J. W. (1961). Interplanetary magnetic field and the auroral zones. *Physical Review Letters*, *6*(2), 47–48. https://doi.org/10.1103/physrevlett.6.47

Franci, L., Hellinger, P., Matteini, L., Verdini, A., & Landi, S. (2016). Two-dimensional hybrid simulations of kinetic plasma turbulence: Current and vorticity vs proton temperature. *AIP Conference Proceedings*, *1720*(1), 040003. https://doi.org/10.1063/1.4943814

Huba, J. D. (1996). The kelvin-Helmholtz instability: Finite Larmor radius magnetohydrodynamics. *Geophysical Research Letters*, *23*(21), 2907–2910. https://doi.org/10.1029/96GL02767

Markovskii, S. A., Vasquez, B. J., Smith, C. W., & Hollweg, J. V. (2006). Dissipation of the perpendicular turbulent cascade in the solar wind. *The Astrophysical Journal*, *639*(2), 1177–1185. https://doi.org/10.1086/499398

McFadden, J. P., Carlson, C. W., Larson, D., Ludlam, M., Abiad, R., Elliott, B., et al. (2008). The THEMIS ESA plasma instrument and in-flight calibration. *Space Science Reviews*, *141*, 277–302. https://doi.org/10.1007/s11214-008-9440-2

Merkin, V. G., Panov, E. V., Sorathia, K. A., & Ukhorskiy, A. Y. (2019). Contribution of bursty bulk flows to the global dipolarization of the magnetotail during an isolated substorm. *Journal of Geophysical Research: Space Physics*, *124*(11), 8647–8668. https://doi.org/10.1029/2019JA026872

Nakamura, R., Baumjohann, W., Klecker, B., Bogdanova, Y., Balogh, A., Rème, H., et al. (2002). Motion of the dipolarization front during a flow burst event observed by Cluster. *Geophysical Research Letters*, *29*, 1942. https://doi.org/10.1029/2002GL015763

Panov, E. V., Baumjohann, W., Nakamura, R., Pritchett, P. L., Weygand, J. M., & Kubyshkina, M. (2019). Ionospheric footprints of detached magnetotail interchange heads. *Geophysical Research Letters*, *46*, 7237–7247. https://doi.org/10.1029/2019GL083070

Panov, E. V., Lu, S., & Pritchett, P. L. (2020). Understanding spacecraft trajectories through detached magnetotail interchange heads. *Journal of Geophysical Research: Space Physics*, *125*, e2020JA027930. https://doi.org/10.1029/2020JA027930

Panov, E. V., Nakamura, R., Baumjohann, W., Kubyshkina, M., Artemyev, A., Sergeev, V. A., et al. (2012). Kinetic ballooning/interchange instability in a bent plasma sheet. *Journal of Geophysical Research*, *117*, A06228. https://doi.org/10.1029/2011JA017496

Panov, E. V., & Pritchett, P. L. (2018a). Dawnward drifting interchange heads in the earth's magnetotail. *Geophysical Research Letters*, *45*(17), 8834–8843. https://doi.org/10.1029/2018GL078482

Panov, E. V., & Pritchett, P. L. (2018b). Ion cyclotron waves rippling ballooning/InterChange instability heads. *Journal of Geophysical Research: Space Physics*, *123*(10), 8261–8274. https://doi.org/10.1029/2018JA025603

Panov, E. V., Sergeev, V. A., Pritchett, P. L., Coroniti, F. V., Nakamura, R., et al. (2012). Observations of kinetic ballooning/interchange instability signatures in the magnetotail. *Geophysical Research Letters*, *39*, L08110. https://doi.org/10.1029/2012GL051668

Parashar, T. N., & Matthaeus, W. H. (2016). Propinquity of current and vortex structures: Effects on collisionless plasma heating. *The Astrophysical Journal*, *832*(1), 57. https://doi.org/10.3847/0004-637x/832/1/57

Perraut, S., Le Contel, O., Roux, A., & Pedersen, A. (2000). Current-driven electromagnetic ion cyclotron instability at substorm onset. *Journal of Geophysical Research*, *105*, 21097–21107. https://doi.org/10.1029/2000JA900059

Pritchett, P. L. (2015). Structure of exhaust jets produced by magnetic reconnection localized in the out-of-plane direction. *Journal of Geophysical Research*, *120*, 592–608. https://doi.org/10.1002/2014JA020795

Pritchett, P. L., & Coroniti, F. V. (2010). A kinetic ballooning/interchange instability in the magnetotail. *Journal of Geophysical Research*, *115*, A06301. https://doi.org/10.1029/2009JA014752

Pritchett, P. L., & Coroniti, F. V. (2011). Plasma sheet disruption by interchange-generated flow intrusions. *Geophysical Research Letters*, *38*, L10102. https://doi.org/10.1029/2011GL047527

Pritchett, P. L., & Coroniti, F. V. (2013). Structure and consequences of the kinetic ballooning/interchange instability in the magnetotail. *Journal of Geophysical Research*, *118*, 146–159. https://doi.org/10.1029/2012JA018143

Pritchett, P. L., Coroniti, F. V., & Nishimura, Y. (2014). The kinetic ballooning/interchange instability as a source of dipolarization fronts and auroral streamers. *Journal of Geophysical Research*, *119*, 4723–4739. https://doi.org/10.1002/2014JA019890

Pritchett, P. L., & Runov, A. (2017). The interaction of finite-width reconnection exhaust jets with a dipolar magnetic field configuration. *Journal of Geophysical Research: Space Physics*, *122*, 3183–3200. https://doi.org/10.1002/2016JA023784

Rosenbluth, M. N., & Longmire, C. L. (1957). Stability of plasmas confined by magnetic fields. *Annals of Physics*, *1*, 120–140. https://doi.org/10.1016/0003-4916(57)90055-6

Rosenbluth, M. N., & Simon, A. (1965). Finite larmor radius equations with nonuniform electric fields and velocities. *The Physics of Fluids*, *8*(7), 1300–1322. https://doi.org/10.1063/1.1761402

Russell, C. T., Khurana, K. K., Huddleston, D. E., & Kivelson, M. G. (1998). Localized reconnection in the near Jovian magnetotail. *Science*, *280*, 1061–1064. https://doi.org/10.1126/science.280.5366.1061

Russell, C. T., Mellott, M. M., Smith, E. J., & King, J. H. (1983). Multiple spacecraft observations of interplanetary shocks: Four spacecraft determination of shock normals. *Journal of Geophysical Research: Space Physics*, *88*(A6), 4739–4748. https://doi.org/10.1029/JA088iA06p04739

Sergeev, V., Angelopoulos, V., Apatenkov, S., Bonnell, J., Ergun, R., Nakamura, R., et al. (2009). Kinetic structure of the sharp injection/dipolarization front in the flow-braking region. *Geophysical Research Letters*, *36*(21), L21105. https://doi.org/10.1029/2009GL040658

Stasiewicz, K. (1993). Finite Larmor radius effects in the magnetosphere. *Space Science Reviews*, *65*(3–4), 221–252. https://doi.org/10.1007/BF00754509

Sundberg, T., Slavin, J. A., Boardsen, S. A., Anderson, B. J., Korth, H., Ho, G. C., et al. (2012). MESSENGER observations of dipolarization events in Mercury's magnetotail. *Journal of Geophysical Research*, *117*, A00M03. https://doi.org/10.1029/2012JA017756

Vasyliunas, V. M. (1983). Plasma distribution and flow. In A. J. Dessler (Ed.), *Physics of the Jovian magnetosphere* (pp. 395–453). https://doi.org/10.1017/cbo9780511564574.013

Yang, Y., Matthaeus, W. H., Parashar, T. N., Haggerty, C. C., Roytershteyn, V., Daughton, W., et al. (2017). Energy transfer, pressure tensor, and heating of kinetic plasma. *Physics of Plasmas*, *24*(7), 072306. https://doi.org/10.1063/1.4990421

## References From the Supporting Information

Pritchett, P. L., & Coroniti, F. V. (1998). Interchange instabilities and localized high-speed flows in the convectively-driven near-Earth plasma sheet. In S. Kokubun, & Y. Kamide (Eds.), *Substorms-4* (pp. 443–448). Kluwer Acad. Publ. https://doi.org/10.1007/978-94-011-4798-9_93

Pritchett, P. L., Coroniti, F. V., Pellat, R., & Karimabadi, H. (1991). Collisionless reconnection in two-dimensional magnetotail equilibria. *Journal of Geophysical Research*, *96*, 11523. https://doi.org/10.1029/91JA01094

Schindler, K., & Birn, J. (2004). MHD stability of magnetotail equilibria including a background pressure. *Journal of Geophysical Research*, *109*, A10208. https://doi.org/10.1029/2004JA010537